On phase transformation models for thermo-mechanically coupled response of Nitinol

Arkaprabha SENGUPTA,[*] Panayiotis PAPADOPOULOS,[†] Aaron KUECK,[‡] and Alan R. PELTON[§]

Table of contents

Abstract

Fully-coupled thermomechanical models for Nitinol at the grain level are developed in this work to capture the inter-dependence between deformation and temperature under non-isothermal conditions. The martensite transformation equations are solved using a novel algorithm which imposes all relevant constraints on the volume fractions. The numerical implementation of the resulting models within the finite element method is effected by the monolithic solution of the momentum and energy equations. Validation of the models is achieved by means of thin-tube experiments at different strain rates.

Keywords: Phase transformation; Nitinol; thermomechanics; finite elements; monolithic solution

---

[*]Department of Mechanical Engineering, University of California, Berkeley
[†]Department of Mechanical Engineering, University of California, Berkeley, corresponding author
[‡]Nitinol Devices & Components, Inc.
[§]Nitinol Devices & Components, Inc.

1 Introduction

The increasing use of shape-memory alloys in technological applications has led to the development of several continuum-level micromechanics-based models of coherent martensitic phase transformation. Models which are restricted to infinitesimal deformations typically adopt an additive decomposition of the total Lagrangian strain into elastic and transformation counterparts [1–4].

In finite deformations, some models employ a multiplicative decomposition of the total deformation gradient into the elastic and transformational counterparts akin to finite plasticity [5–7], while others do not explicitly require such a decomposition [8, 9]. Existence and invariance issues related to the use of an intermediate configuration essential to this decomposition are discussed in [10]. There, it is argued that, unlike plasticity, an intermediate configuration can be locally attained by thermomechanical (as opposed to purely mechanical) unloading and that, similarly to certain treatments of plasticity [11], an isoclinic configuration induced by the austenite lattice may be used to resolve the matter of invariance. Some of the existing models include the full coupling between mechanical and thermal effects [5, 6, 12], which is particularly important in problems that involve non-isothermal loading. However, none of the aforementioned works report direct comparisons between predicted and experimentally measured stress-temperature results at different rates of loading.

The current work proposes two constitutive models for the fully-coupled thermomechanical behavior of shape-memory alloys. One of the models is based on a physically motivated multiplicative decomposition of the total deformation gradient at the mesoscale [10], while the other constitutes an extension to the purely mechanical approach advocated in [9]. In essence, the former includes the effect of local rotations (at grain level) induced by the transformation deformation, while the latter neglects this effect altogether. The study of two models enables an assessment of the significance of including these rotations in the prediction of stresses and temperatures during phase transformation. Further, a novel algorithmic scheme is devised to solve the resulting transformation equations subject to all the necessary constraints. This scheme starts with a set of potentially active variants, but instead of enforcing the constraints *a posteriori* on the volume fractions as in [13], uses a predictor-corrector approach which iteratively solves the constraint equations simultaneously with the transformation equations until both are exactly satisfied. A monolithic finite element formulation is subsequently employed to solve the momentum and energy

equations using a Newton-Raphson scheme, while selectively ignoring some of the weak couplings in the governing equations in order to simplify the consistent algorithmic tangents. Further, the evolution of temperature under mechanical loading at moderate strain rates and its effect on the constitutive response are investigated. The latter effect has been observed earlier in experiments on CuAl [14] and NiTi [15, 16] shape-memory alloys. While this has been modeled in previous works [5, 12], the numerical results have not been quantitatively compared to experiments. Here, experiments on thin-walled tubes at different strain rates are initially used to estimate some of the material parameters and the heat transfer coefficient due to convection between the specimen and air. Subsequently, the simulation results are compared to a wider set of experiments for validation purposes.

The organization of this paper is as follows: Section 2 includes background on the kinematics and kinetics of phase transformation at the grain level. This is followed by the constitutive development in Section 3 and the algorithmic treatment of the transformation equations in Section 4. The finite element implementation, including the linearization of the governing equations of motion is presented in Section 5, while numerical and experimental results are introduced and compared in Section 6. Concluding remarks are included in Section 7.

2 Kinematics and balance laws of mesoscale martensitic phase transformation

2.1 Kinematics

The microstructure of a crystal grain in a material undergoing martensitic phase transition comprises subdomains of untransformed austenite and habit-plane variants of martensite. The overall deformation of the grain may be characterized through homogenization of the deformation in these subdomains. In the model presented here, the mesoscale total deformation gradient is decomposed multiplicatively into elastic and transformation counterparts. The theoretical underpinnings of the use of this decomposition in the context of martensitic phase transformations has been discussed at length in [10]. This decomposition is mathematically expressed as

$$\mathbf{F} = \mathbf{F}^e \mathbf{F}^t , \tag{1}$$

where $\mathbf{F}^e$ and $\mathbf{F}^t$ are the elastic and transformation deformation gradients. The total transformation deformation gradient is expressed in terms of the transformation gradients

$\mathbf{F}_\alpha^t$, $\alpha = 1, 2, \ldots, nv$, associated with each of the nv habit-plane martensitic variants as

$$\mathbf{F}^t = (1 - \sum_{\alpha=1}^{nv} \xi_\alpha)\mathbf{I} + \sum_{\alpha=1}^{nv} \xi_\alpha \mathbf{F}_\alpha^t . \tag{2}$$

Here, ξ_α is the volume fraction of the α-th martensitic variant and $\mathbf{I}$ is the second-order identity tensor corresponding to the transformation deformation gradient of the parent austenite phase [10]. The kinematics of the solid-solid phase transformation requires that

$$\mathbf{F}_\alpha^t = \mathbf{I} + \mathbf{H}_\alpha^t , \tag{3}$$

where the displacement gradient $\mathbf{H}_\alpha^t$ for the variant α is written in terms of the habit-plane displacement $\mathbf{b}_\alpha$ and the corresponding habit-plane normal $\mathbf{m}_\alpha$ as $\mathbf{H}_\alpha^t = \mathbf{b}_\alpha \otimes \mathbf{m}_\alpha$. It follows from (2) and (3) that

$$\mathbf{F}^t = \hat{\mathbf{F}}^t(\{\xi_\alpha\}) = \mathbf{I} + \sum_{\alpha=1}^{nv} \xi_\alpha \mathbf{H}_\alpha^t . \tag{4}$$

Hence, the rate of the transformation decomposition gradient is given by

$$\dot{\mathbf{F}}^t = \sum_{\alpha=1}^{nv} \dot{\xi}_\alpha \mathbf{H}_\alpha^t , \tag{5}$$

where it is assumed that the reference configuration of the underlying austenite lattice remains unchanged with respect to the laboratory frame of reference.

Given the elastic deformation gradient in (1), the elastic Green-Lagrange strain relative to the intermediate configuration induced by $\mathbf{F}^t$ is

$$\mathbf{E}^e = \frac{1}{2}(\mathbf{C}^e - \mathbf{I}) = \frac{1}{2}(\mathbf{F}^{eT}\mathbf{F}^e - \mathbf{I}) = \frac{1}{2}(\mathbf{F}^{t-T}\mathbf{C}\mathbf{F}^{t-1} - \mathbf{I}) , \tag{6}$$

where $\mathbf{C}(= \mathbf{F}^T\mathbf{F})$ is the right Cauchy-Green deformation tensor and $\mathbf{C}^e(= \mathbf{F}^{eT}\mathbf{F}^e)$ is its elastic counterpart. Therefore, the rate of change of the elastic Green-Lagrange strain becomes

$$\dot{\mathbf{E}}^e = \frac{1}{2}(\dot{\mathbf{F}}^{eT}\mathbf{F}^e + \mathbf{F}^{eT}\dot{\mathbf{F}}^e) . \tag{7}$$

2.2 Balance laws

The linear and angular momentum balance equations are written in local referential form as

$$\begin{aligned}
\mathrm{Div}\mathbf{P} + \rho_0 \mathbf{f} &= \rho_0 \mathbf{a} , \\
\mathbf{P}\mathbf{F}^T &= \mathbf{F}\mathbf{P}^T ,
\end{aligned} \tag{8}$$

where $\mathbf{P}$ is the first Piola-Kirchhoff stress tensor, ρ_0 is the mass density per unit referential volume, $\mathbf{f}$ is the body force per unit mass, and $\mathbf{a}$ is the acceleration. In addition, the energy balance equation takes the form

$$\rho_0 \dot{\epsilon} = \rho_0 r - \mathrm{Div}\mathbf{q}_0 + \mathbf{P} \cdot \dot{\mathbf{F}} , \tag{9}$$

in terms of the internal energy per unit mass ϵ, the heat supply per unit mass r, and the heat flux vector $\mathbf{q}_0$ resolved over the geometry of the reference configuration. Appealing to the multiplicative decomposition in (1), the stress power term in (9) can be expanded to

$$\mathbf{P} \cdot \dot{\mathbf{F}} = \mathbf{P} \cdot (\dot{\mathbf{F}}^e \mathbf{F}^t + \mathbf{F}^e \dot{\mathbf{F}}^t) . \tag{10}$$

Taking into account (1) and (7), the term on the right-hand side of (10) that involves the rate of the elastic deformation gradient can be written as

$$\mathbf{P} \cdot (\dot{\mathbf{F}}^e \mathbf{F}^t) = \mathbf{S}^e \cdot \dot{\mathbf{E}}^e , \tag{11}$$

where $\mathbf{S}^e$ is a symmetric tensor given by

$$\mathbf{S}^e = \mathbf{F}^{e-1} \mathbf{P} \mathbf{F}^{tT} = \mathbf{F}^t \mathbf{S} \mathbf{F}^{tT} \tag{12}$$

and $\mathbf{S}$ ($= \mathbf{F}^{-1}\mathbf{P}$) is the second Piola-Kirchhoff stress. Hence, $\mathbf{S}^e$ is the push-forward of second Piola-Kirchhoff stress to the intermediate configuration. Therefore, the quantity in (11) is understood to be the elastic power. Furthermore, with the aid of (4) the second term on the right-hand side of (10) can be expressed as

$$\mathbf{P} \cdot (\mathbf{F}^e \dot{\mathbf{F}}^t) = \sum_{\alpha=1}^{nv} (\mathbf{F}^{eT}\mathbf{P}) \cdot (\dot{\xi}_\alpha \mathbf{H}^t_\alpha) = \sum_{\alpha=1}^{nv} (\mathbf{F}^{eT}\mathbf{P}^e) \cdot (\mathbf{H}^t_\alpha \mathbf{F}^{t-1})\dot{\xi}_\alpha , \tag{13}$$

where, upon recalling (12),

$$\mathbf{P}^e = \mathbf{P}\mathbf{F}^{tT} = \mathbf{F}^e \mathbf{S}^e \tag{14}$$

is the push-forward of $\mathbf{P}$ to the intermediate configuration. Denoting by τ_α the work-conjugate kinetic quantity to ξ_α, namely setting $\tau_\alpha = (\mathbf{F}^{eT}\mathbf{P}^e) \cdot (\mathbf{H}^t_\alpha \mathbf{F}^{t-1}) = (\mathbf{C}^e \mathbf{S}^e) \cdot (\mathbf{H}^t_\alpha \mathbf{F}^{t-1})$, it follows that

$$\mathbf{P} \cdot (\mathbf{F}^e \dot{\mathbf{F}}^t) = \sum_{\alpha=1}^{nv} \tau_\alpha \dot{\xi}_\alpha . \tag{15}$$

It is clear that the term in (13) quantifies the inelastic power and contributes to dissipation, as will be seen in Section 3.1. Taking into account (10), (11), (15) and the definition of $\mathbf{S}$, the energy equation (9) may be rewritten as

$$\rho_0 \dot{\epsilon} = \rho_0 r - \mathrm{Div}\mathbf{q}_0 + \mathbf{S} \cdot \dot{\mathbf{E}} = \rho_0 r - \mathrm{Div}\mathbf{q}_0 + \mathbf{S}^e \cdot \dot{\mathbf{E}}^e + \sum_{\alpha=1}^{nv} \tau_\alpha \dot{\xi}_\alpha . \tag{16}$$

Finally, a local referential form of the Clausius-Duhem inequality may be stated as

$$\rho_0 \dot{\eta} \theta \geq \rho_0 r - \operatorname{Div} \mathbf{q}_0 + \frac{\mathbf{q}_0 \cdot \operatorname{Grad} \theta}{\theta} , \tag{17}$$

where Grad denotes gradient relative to the referential coordinates.

3 Thermomechanical Constitutive Modeling for Phase Transformation

3.1 A new thermomechanical model

In this section, a Helmholtz free energy is proposed for the phase transformation of Nitinol by adding together all relevant entropic, thermomechanical, and chemical contributions. To this end, recall that the Helmholtz free energy is related to the internal the internal energy ϵ and the entropy η by

$$\Psi = \rho_0 (\epsilon - \eta \theta) . \tag{18}$$

Next, assume that the internal energy and the entropy depend on the elastic Green-Lagrange strain $\mathbf{E}^e$, the volume fractions $\{\xi_\alpha\}$ of the martensite variants (which characterize the transformation state), and the absolute temperature θ. By virtue of (18), this means that the free energy is expressed as $\Psi = \bar{\Psi}(\mathbf{E}^e, \{\xi_\alpha\}, \theta)$. Appealing to $(16)_2$, (18) and the constitutive dependencies of $\bar{\Psi}$, the Clausius-Duhem inequality (17) results in

$$\left(\frac{\partial \bar{\Psi}}{\partial \mathbf{E}^e} - \mathbf{S}^e \right) \cdot \dot{\mathbf{E}}^e + \left(\frac{\partial \bar{\Psi}}{\partial \theta} + \rho_0 \eta \right) \dot{\theta} + \sum_{\alpha=1}^{nv} \left(\frac{\partial \bar{\Psi}}{\partial \xi_\alpha} - \tau_\alpha \right) \dot{\xi}_\alpha + \frac{\mathbf{q}_0 \cdot \operatorname{Grad} \theta}{\theta} \leq 0 . \tag{19}$$

Since there exist purely thermoelastic processes (i.e., such that $\dot{\xi}_\alpha = 0$) at any state $(\mathbf{E}^e, \{\xi_\alpha\}, \theta)$, the standard Coleman-Noll argument may be applied to the preceding equation and leads to

$$\mathbf{S}^e = \frac{\partial \bar{\Psi}}{\partial \mathbf{E}^e} \quad , \quad \rho_0 \eta = -\frac{\partial \bar{\Psi}}{\partial \theta} \quad , \quad -\sum_{\alpha=1}^{nv} \left(\frac{\partial \bar{\Psi}}{\partial \xi_\alpha} - \tau_\alpha \right) \dot{\xi}_\alpha \geq 0 \quad , \quad \frac{\mathbf{q}_0 \cdot \operatorname{Grad} \theta}{\theta} \leq 0 . \tag{20}$$

Note that the term $\tau_\alpha \dot{\xi}_\alpha$ in $(20)_3$ contributes to the dissipation due to the phase transformation.

Equations $(6)_3$ and (4) reveal that the elastic Green-Lagrange strain $\mathbf{E}^e$ can be written as a function of $\mathbf{E}$ and $\{\xi_\alpha\}$. Therefore, the Helmholtz free energy may be expressed as a function of $\mathbf{E}$, $\{\xi_\alpha\}$ and θ, namely

$$\Psi = \bar{\Psi}(\mathbf{E}^e(\mathbf{E}, \{\xi_\alpha\}), \{\xi_\alpha\}, \theta) = \hat{\Psi}(\mathbf{E}, \{\xi_\alpha\}, \theta) . \tag{21}$$

This demonstrates that, in the context of the proposed model, the phase-transforming material may be viewed as an *nv*-parameter family of thermoelastic materials induced by the set of martensite volume fractions $\{\xi_\alpha\}$.

The constitutive equations (20) can be alternatively derived from the Helmholtz free energy function $\hat{\Psi}(\mathbf{E}, \{\xi_\alpha\}, \theta)$. Indeed, using $(16)_1$ and (18) and recalling the constitutive dependencies of $\hat{\Psi}$, the Clausius-Duhem inequality (17) leads to

$$\left(\frac{\partial\hat{\Psi}}{\partial\mathbf{E}} - \mathbf{S}\right) \cdot \dot{\mathbf{E}} + \left(\frac{\partial\hat{\Psi}}{\partial\theta} + \rho_0\eta\right)\dot{\theta} + \sum_{\alpha=1}^{nv} \frac{\partial\hat{\Psi}}{\partial\xi_\alpha}\dot{\xi}_\alpha + \frac{\mathbf{q}_0 \cdot \operatorname{Grad}\theta}{\theta} \leq 0 . \tag{22}$$

The Coleman-Noll procedure now yields the constitutive relations

$$\mathbf{S} = \frac{\partial\hat{\Psi}}{\partial\mathbf{E}} \quad , \quad \rho_0\eta = -\frac{\partial\hat{\Psi}}{\partial\theta} \quad , \quad -\sum_{\alpha=1}^{nv} \frac{\partial\hat{\Psi}}{\partial\xi_\alpha} \dot{\xi}_\alpha \geq 0 \quad , \quad \frac{\mathbf{q}_0 \cdot \operatorname{Grad}\theta}{\theta} \leq 0 . \tag{23}$$

Note that $(23)_{1,2}$ are identical in structure to the constitutive equations of a thermoelastic solid. Also, the left-hand side of $(23)_3$ represents the dissipation generated during phase transformation by the driving forces $f_\alpha = -\dfrac{\partial\hat{\Psi}}{\partial\xi_\alpha}$. It can be now verified using (18), $(16)_1$ and $(23)_{1,2}$ that the rate of entropy satisfies the relation

$$\rho_0\dot{\eta}\theta = \rho_0 r - \operatorname{Div}\mathbf{q}_0 + \sum_{\alpha=1}^{nv} f_\alpha\dot{\xi}_\alpha . \tag{24}$$

A specific choice of the Helmholtz free energy functional is now proposed. The entropic part of the energy involves only thermal effects due to temperature changes with respect to a reference temperature θ_0, chosen here to be the ambient temperature. This contribution is typically ignored for quasi-static mechanical loading, where isothermal conditions are assumed. To define the entropic part, let the volumetric heat capacity c at a given elastic Green-Lagrange strain and transformation state be

$$c = \hat{c}(\mathbf{E}^e, \{\xi_\alpha\}, \theta) = \rho_0\frac{\partial\epsilon(\mathbf{E}^e, \{\xi_\alpha\}, \theta)}{\partial\theta} = \rho_0\theta\frac{\partial\eta(\mathbf{E}^e, \{\xi_\alpha\}, \theta)}{\partial\theta} , \tag{25}$$

where (18) and $(20)_3$ are used in deriving $(25)_2$. Integrating the equations in (25) from θ_0 to θ yields the thermal parts of the internal energy and entropy as

$$\rho_0\big(\epsilon(\mathbf{E}^e, \{\xi_\alpha\}, \theta) - \epsilon(\mathbf{E}^e, \{\xi_\alpha\}, \theta_0)\big) = \int_{\theta_0}^{\theta} \hat{c}(\mathbf{E}^e, \{\xi_\alpha\}, \vartheta) \, d\vartheta \tag{26}$$

and

$$\rho_0\big(\eta(\mathbf{E}^e, \{\xi_\alpha\}, \theta) - \eta(\mathbf{E}^e, \{\xi_\alpha\}, \theta_0)\big) = \int_{\theta_0}^{\theta} \frac{\hat{c}(\mathbf{E}^e, \{\xi_\alpha\}, \vartheta)}{\vartheta} \, d\vartheta . \tag{27}$$

The Helmholtz free energy is deduced from (18), (26) and (27) by assuming that the function $\hat{c}(\mathbf{E}^e, \{\xi_\alpha\}, \vartheta)$ is constant and equal to c. In this case, one may write

$$\bar{\Psi}(\mathbf{E}^e, \{\xi_\alpha\}, \theta) = \rho_0\big(\epsilon(\mathbf{E}^e, \{\xi_\alpha\}, \theta_0) - \eta(\mathbf{E}^e, \{\xi_\alpha\}, \theta_0)\theta\big) + c\left(\theta - \theta_0 - \theta \log\left(\frac{\theta}{\theta_0}\right)\right) . \quad (28)$$

The thermomechanical part of the free energy is assumed to satisfy the two basic relations

$$\frac{\partial^2 \bar{\Psi}}{\partial \mathbf{E}^e \partial \mathbf{E}^e} = \mathbb{C} \quad , \qquad \frac{\partial^2 \bar{\Psi}}{\partial \mathbf{E}^e \partial \theta} = -\mathbb{C}\mathbf{A} . \quad (29)$$

Here, $\mathbb{C}$ is the fourth-order elastic modulus tensor given by

$$\mathbb{C} = (1 - \sum_{\alpha=1}^{nv} \xi_\alpha)\mathbb{C}_a + \sum_{\alpha=1}^{nv} \xi_\alpha \mathbb{C}_m , \quad (30)$$

in terms of the respective elastic moduli $\mathbb{C}_a$ and $\mathbb{C}_m$ of the austenite and martensite phases. Also, $\mathbf{A}$ is the second-order thermal expansion tensor, assumed here to be constant. Lastly, the chemical part of free energy is taken to be a linear function of both the deviation of temperature from a thermodynamic equilibrium temperature θ_T between the austenite and martensite phases and the total martensitic volume fraction. In summary, the Helmholtz free energy takes the form

$$\Psi = \bar{\Psi}(\mathbf{E}^e, \{\xi_\alpha\}, \theta) = \frac{1}{2}\mathbf{E}^e \cdot \mathbb{C}\mathbf{E}^e - \mathbf{E}^e \cdot \mathbb{C}\mathbf{A}(\theta - \theta_0) + B(\theta - \theta_T)\sum_{\alpha=1}^{nv} \xi_\alpha$$
$$+ c\left(\theta - \theta_0 - \theta \log\left(\frac{\theta}{\theta_0}\right)\right) , \quad (31)$$

where $B(> 0)$ is the chemical energy coefficient. Note that the energy due to interaction between martensitic variants is neglected in this model. A Helmholtz free energy of the functional form (31) has been proposed in [5], albeit starting from a completely different definition of $\mathbf{F}^t$ (thus leading to a different definition of the state variable $\mathbf{E}^e$). The relation between the two models is discussed further in Section 3.2.

An expression for the stress $\mathbf{S}$ may be obtained from $(23)_1$ with the aid of $(20)_1$, (31), (21) $(6)_3$ and the chain rule, as

$$\mathbf{S} = \left(\frac{\partial \mathbf{E}^e}{\partial \mathbf{E}}\right)^T \frac{\partial \bar{\Psi}}{\partial \mathbf{E}^e} = \mathbf{F}^{t-1}\mathbf{S}^e\mathbf{F}^{t-T} , \quad (32)$$

where

$$\mathbf{S}^e = \mathbb{C}\big(\mathbf{E}^e - \mathbf{A}(\theta - \theta_0)\big) . \quad (33)$$

Likewise, the entropy η is obtained from $(20)_2$ and (31) as

$$\rho_0 \eta \;=\; \mathbf{E}^e \cdot \mathbb{C}\mathbf{A} - B \sum_{\alpha=1}^{nv} \xi_\alpha + c \, \log\left(\frac{\theta}{\theta_0}\right) \; . \tag{34}$$

Further, the rate of temperature change may be determined upon substituting (34) into (24) as

$$c\dot{\theta} \;=\; \rho_0 r + \mathrm{Div}(\mathbf{K}\,\mathrm{Grad}\,\theta) + \sum_{\alpha=1}^{nv}(B\theta + f_\alpha)\dot{\xi}_\alpha - \overline{\mathbf{E}^e \cdot \mathbb{C}\mathbf{A}}\, \theta \; , \tag{35}$$

where Fourier's law is applied by relating the referential flux $\mathbf{q}_0$ to the referential gradient of temperature $\mathrm{Grad}\,\theta$ according to $\mathbf{q}_0 = -\mathbf{K}\,\mathrm{Grad}\,\theta$, in terms of a positive-definite second-order conductivity tensor $\mathbf{K}$.

Forward or reverse transformation is assumed to occur when the thermodynamic driving force f_α conjugate to the martensitic variant with volume fraction ξ_α in the dissipation inequalities $(20)_3$ or $(23)_3$ reaches a critical value, namely

$$f_\alpha \;=\; \begin{cases} \mathcal{F}_c & \text{(forward transformation)} \\ -\mathcal{F}_c & \text{(reverse transformation)} \end{cases} \;, \tag{36}$$

where $\mathcal{F}_c$ is a positive constant. This is a rate-independent transformation law, since the critical value of the driving force is a constant during persistent forward or reverse transformation. It is noted that rate-dependent transformation laws have been proposed for Nitinol to model changes in the thermomechanical response observed at different loading rates, see, e.g., [5, 17]. However, there exists experimental evidence that such changes are principally due to the different temperature evolutions realized in the specimen at different rates of loading, and their direct effect on the transformation of the specimen [16]. This obviates the need for rate-dependent modeling of the transformation laws.

For the proposed model, an expression for the thermodynamic driving force is derived in Appendix A as

$$f_\alpha \;=\; (\mathbf{C}^e\mathbf{S}^e) \cdot \left(\mathbf{H}_\alpha^t \mathbf{F}^{t-1}\right) - B(\theta - \theta_T) \; . \tag{37}$$

The model proposed here will be referred to as the "FT" model, when comparing it with other models discussed in the following section.

3.2 Comparison to other models

Two alternative models of micromechanically-motivated continuum phase transformation are briefly introduced here and compared to the proposed model.

In the work of Anand and Gurtin [5], the Helmholtz free energy is defined as in (31). However, the evolution of the transformation deformation gradient is governed by a rate-type equation of the form

$$\dot{\mathbf{F}}^t = \left(\sum_{\alpha=1}^{nv} \dot{\xi}_\alpha \mathbf{H}_\alpha^t \right) \mathbf{F}^t \ , \tag{38}$$

where the rate of change of the martensite volume fractions is determined by enforcing the conditions (36). This constitutive equation is motivated by the theory of crystallographic slip in metals and, unlike the proposed model, is not amenable to a reduction to a parametrized thermo-elastic solid as in (21). The stress $\mathbf{S}$ in this model is derived from an equation identical in form to (32), albeit with the definition of the transformation deformation gradient as in (38). Also, the thermodynamic force f_α^{AG} for this model is given by

$$f_\alpha^{AG} = \tau_\alpha^{AG} - \frac{\partial \bar{\Psi}}{\partial \xi_\alpha} = (\mathbf{C}^e \mathbf{S}^e) \cdot \mathbf{H}_\alpha^t - B(\theta - \theta_T) \ . \tag{39}$$

Furthermore, the temperature evolution is governed by (35), where the thermodynamic force is given by (39).

A second alternative model by adding the thermomechanical coupling and the entropic terms to the Helmholtz free energy proposed in Jung *et al.* [9]. This results in

$$\Psi = \hat{\Psi}^J(\mathbf{E}, \{\xi_\alpha\}, \theta) = \frac{1}{2}(\mathbf{E} - \mathbf{E}^t) \cdot \mathbb{C}(\mathbf{E} - \mathbf{E}^t) + B(\theta - \theta_T) \sum_{\alpha=1}^{nv} \xi_\alpha - $$
$$(\mathbf{E} - \mathbf{E}^t) \cdot \mathbb{C} \mathbf{A}(\theta - \theta_0) + c \left(\theta - \theta_0 - \theta \log \left(\frac{\theta}{\theta_0} \right) \right) \ , \tag{40}$$

where the transformation Green-Lagrange strain $\mathbf{E}^t$ is defined as

$$\mathbf{E}^t = \sum_{\alpha=1}^{nv} \xi_\alpha \mathbf{E}_\alpha^t \ , \tag{41}$$

in terms of the respective strains $\mathbf{E}_\alpha^t$ of the habit-plane variants of martensite. The strains $\mathbf{E}_\alpha^t$ are derived from the transformation deformation gradients $\mathbf{F}_\alpha^t$ in (3). Hence the rate of $\mathbf{E}^t$ is given by

$$\dot{\mathbf{E}}^t = \sum_{\alpha=1}^{nv} \dot{\xi}_\alpha \mathbf{E}_\alpha^t \ . \tag{42}$$

The stress $\mathbf{S}$ in this model is expressed as

$$\mathbf{S} = \mathbb{C} \left(\mathbf{E} - \mathbf{E}^t - \mathbf{A}(\theta - \theta_0) \right) \ . \tag{43}$$

In addition, the thermodynamic force f_α^J takes the form

$$f_\alpha^J = -\frac{\partial \hat{\Psi}^J}{\partial \xi_\alpha} = \mathbf{E}_\alpha^t \cdot \mathbf{S} - B(\theta - \theta_T) \ , \tag{44}$$

where (43) and (41) have been used. Now, in analogy to the derivation of (35), it can be shown that the evolution of temperature is governed by

$$c\dot{\theta} \;=\; \rho_0 r + \mathrm{Div}(\mathbf{K}\,\mathrm{Grad}\,\theta) + \sum_{\alpha=1}^{nv}\left(B\theta + f_\alpha^J\right)\dot{\xi}_\alpha - \overline{(\mathbf{E}-\mathbf{E}^t)\cdot\mathbb{C}\mathbf{A}}\,\theta \;. \tag{45}$$

The second model presented in this section will be referred to as "ET" model for comparison purposes. As mentioned in Section 1, this model ignores the effect of rotation associated with transformation deformation. The difference in the stress response between this model and the "FT" model will be illustrated through a numerical example in Section 6.1

4 Incremental solution of the transformation equations

In this section, an incremental method is proposed for the solution of the transformation equations (36) subject to the constraint conditions

$$-\xi_\alpha \;\leq\; 0 \qquad , \qquad \sum_{\alpha=1}^{nv}\xi_\alpha \;\leq\; 1 \;. \tag{46}$$

In this method, all variant volume fractions are assumed to be known at time $t = t_n$ and the forward and reverse transformation equations are solved for the new values of the volume fractions at time $t = t_{n+1}$. The proposed solution method includes an active set component to determine and update the set of potentially active martensite variants in $(t_n, t_{n+1}]$ consistently with the transformation conditions (36) and the constraints (46). The algorithm developed here is motivated by the work in [13]. However in contrast to their work, the constraints on the volume fractions are satisfied exactly in this algorithm, and their effect on the transformation equations is taken into consideration.

The proposed algorithm is summarized as follows: First, a potentially active set $\mathcal{PA}$ of transforming variants is determined by calculating trial thermodynamic forces $f_{\alpha,n+1}^{(0)}$ from the present state of strain and temperature, and consists of the variants whose forces exceed the critical values in (36), namely satisfy $\mid f_{\alpha,n+1}^{(0)} \mid \geq \mathcal{F}_c$. Next, the volume fractions of the potentially active variants are determined from the transformation equations (36). These are solved for all variants $\alpha \in \mathcal{PA}$ in either forward transformation (if $f_{\alpha,n+1}^{(0)} \geq \mathcal{F}_c$) or reverse transformation ($f_{\alpha,n+1}^{(0)} \leq -\mathcal{F}_c$). Taking into account (37), the transformation equations take the form

$$\left(\mathbf{C}_{n+1}^e\mathbf{S}_{n+1}^e\right)\cdot\left(\mathbf{H}_\alpha^t\mathbf{F}_{n+1}^{t-1}\right) - B(\theta_{n+1}-\theta_T) \;=\; \pm\mathcal{F}_c \;, \tag{47}$$

and are clearly non-linear in $\{\xi_{\alpha,n+1}\}$. The volume fractions are determined iteratively by linearizing (47) to

$$\sum_{\beta \in \mathcal{PA}} A_{\alpha\beta}(\Delta\xi_\beta) \;=\; b_\alpha \qquad , \qquad \alpha \in \mathcal{PA} \;, \tag{48}$$

and using the Newton-Raphson method. Appendix A contains derivations of explicit expressions for $A_{\alpha\beta}$ and b_α. Note that there is no guarantee that the algebraic system (48) possesses a unique solution, hence a solution based on the pseudo-inverse of the square matrix $[A_{\alpha\beta}]$ is generally required. The active set portion of the solution method is completed by verifying whether the changes of volume fractions in $(t_n, t_{n+1}]$ are in the same direction with the corresponding driving forces, namely whether the discrete counterpart of the dissipation in $(23)_3$ is variant-wise non-negative for all $\alpha \in \mathcal{PA}$. If not, any offending variants are dropped from $\mathcal{PA}$, and a new system of transformation equations is solved until all remaining variants in $\mathcal{PA}$ are consistent with the preceding discrete dissipation condition. The constraint $(46)_2$ is subsequently enforced by scaling the incremental changes of the active variants until it is satisfied. In contrast, violation of $(46)_1$ prompts, again, scaling of the preceding incremental changes until the most offending variant satisfies $(46)_1$ as an equality, followed by the removal of this variant and a new solution of (47). In this manner, the new active variants continue to satisfy the requisite transformation equations. The complete algorithm for the determination of the volume fractions is described in Appendix B.

Define next the functions $\hat{\Phi}^f = \hat{\Psi} + \sum_{\alpha \in \mathcal{J}^f} \mathcal{F}^c \xi_\alpha$ and $\hat{\Phi}^r = \hat{\Psi} - \sum_{\alpha \in \mathcal{J}^r} \mathcal{F}^c \xi_\alpha$, where $\mathcal{J}^f$ and $\mathcal{J}^r$ are the sets of variants in forward and reverse transformation that satisfy $(36)_{1,2}$, respectively. For the constitutive model in (40), the functions $\hat{\Phi}^f$ and $\hat{\Phi}^r$ attain non-unique global minima during forward or reverse transformation at a given strain and temperature. This conclusion can be readily deduced from (36) and holds true provided that the elastic modulus $\mathbb{C}$ is constant and the Hessian of $\hat{\Phi}^f$ and $\hat{\Phi}^r$ is positive-semidefinite, see [9] for details. The minimization of $\hat{\Phi}^f$ and $\hat{\Phi}^r$ is subject to the constraints conditions of the form

$$-\xi_\alpha \;\leq\; 0 \qquad , \qquad \bar{\xi}_l - \sum_{\alpha=1}^{nv} \xi_\alpha \;\leq\; 0 \qquad , \qquad \sum_{\alpha=1}^{nv} \xi_\alpha - \bar{\xi}_u \;\leq\; 0 \;. \tag{49}$$

In case of elastic loading/unloading or forward transformation from a state with initial total martensitic volume fraction ξ_{total}, it is clear that $\bar{\xi}_l = \xi_{total}$ and $\bar{\xi}_u = 1$. Likewise, in case of elastic loading/unloading or reverse transformation, $\bar{\xi}_l = 0$ and $\bar{\xi}_u = \xi_{total}$, see [9] for further details of an algorithmic implementation using an active set strategy.

Unfortunately, no such minimization problem can be formulated for the model in (31), since the Hessian associated with this free energy is not necessarily positive-definite.

5 Finite Element Implementation

The finite element formulation of the coupled thermomechanical problem is based on the use of the classical Galerkin method. To wit, let Ω_0 be the region occupied by the body in the reference configuration and denote by $\partial\Omega_0$ its smooth and orientable boundary having outward unit normal $\mathbf{N}$. Also, let the boundary be decomposed into parts $\Gamma_{u,0}^m$ and $\Gamma_{p,0}^m$, where Dirichlet and Neumann boundary conditions are enforced for the momentum equations, as well as into parts $\Gamma_{u,0}^t$ and $\Gamma_{p,0}^t$, where Dirichlet and Neumann boundary conditions are enforced for the energy equation.

The weak statement of linear momentum balance takes the familiar form

$$\int_{\Omega_0} \frac{\partial \mathbf{w}}{\partial \mathbf{X}} \cdot \mathbf{P} \, dV \;=\; \int_{\Gamma_{p,0}^m} \mathbf{w} \cdot \bar{\mathbf{p}} \, dA + \int_{\Omega_0} \mathbf{w} \cdot \rho_0 (\mathbf{f} - \mathbf{a}) \, dV \;, \tag{50}$$

where $\mathbf{w}$ is the H_1-smooth vector weighting function that vanishes on $\Gamma_{u,0}^m$ and $\bar{\mathbf{p}} = \mathbf{P}\mathbf{N}$ is the prescribed traction resolved on the geometry of the reference configuration. Likewise, the weak form of the energy equation (35) for the primary model proposed here is derived easily as

$$\int_{\Omega_0} w \, c \, \dot{\theta} \, dV + \int_{\Omega_0} \mathrm{Grad}\, w \cdot \mathbf{K} \, \mathrm{Grad}\, \theta \, dV + \int_{\Omega_0} w \, \overline{\mathbf{E}^e \cdot \mathbb{C}\mathbf{A}} \, \theta \, dV$$
$$- \int_{\Omega_0} w \, \sum_{\alpha=1}^{nv} \left[\left(B\theta_T + (\mathbf{C}^e \mathbf{S}^e) \cdot \left(\mathbf{H}_\alpha^t \mathbf{F}^{t-1} \right) \right) \dot{\xi}_\alpha \right] dV \;=\;$$
$$\int_{\Omega_0} w \, \rho_0 r \, dV - \int_{\Gamma_{p,0}^t} w \bar{h} \, dA \;, \quad (51)$$

where w is the H^1-smooth scalar weighting function that vanishes on $\Gamma_{u,0}^t$, $\bar{h} = \mathbf{q}_0 \cdot \mathbf{N}$ is the prescribed heat flux on $\Gamma_{p,0}^t$. Also, the last term of the left-hand side is obtained by substituting the expression for the thermodynamic force f_α from (37).

Similarly, for the second model, the weak statement of the energy equation (45) is given

by

$$\int_{\Omega_0} w c \dot{\theta} \, dV + \int_{\Omega_0} \text{Grad} \, w \cdot \mathbf{K} \, \text{Grad} \, \theta \, dV + \int_{\Omega_0} w \overline{(\mathbf{E} - \mathbf{E}^t) \cdot \mathbb{C} \mathbf{A}} \theta \, dV$$

$$- \int_{\Omega_0} w \sum_{\alpha=1}^{nv} \left[\left(B \theta_T + \mathbf{E}_\alpha^t \cdot \mathbf{S} \right) \dot{\xi}_\alpha \right] dV =$$

$$\int_{\Omega_0} w \, \rho_0 r \, dV - \int_{\Gamma_{p,0}^t} w \bar{h} \, dA \ , \quad (52)$$

where, again, use is made of the expression for the thermodynamic force in (44).

The residual and tangent terms for the preceding equations are derived henceforth. Note that in order to simplify the computation of tangents, the transformation deformation gradient and the homogenized elastic modulus are evaluated approximately in terms of the volume fractions of previous time-step. Indeed, recalling (4) and (30), it is assumed that

$$\mathbf{F}_{n+1}^t \ \dot{=} \ \mathbf{I} + \sum_{\alpha=1}^{nv} \xi_{\alpha,n} \, \mathbf{H}_\alpha^t \ , \quad (53)$$

and

$$\mathbb{C}_{n+1} \ \dot{=} \ \left[(1 - \sum_{\alpha=1}^{nv} \xi_{\alpha,n}) \mathbb{C}_a + \sum_{\alpha=1}^{nv} \xi_{\alpha,n} \mathbb{C}_m \right] . \quad (54)$$

These explicit approximations induce an error in the solution of the governing equations that can be controlled by the size of the time-step.

The finite element interpolations for displacement and temperature may be expressed as

$$u_a = \ \sum_I N^I \, u_a^I \quad , \quad \theta = \sum_I N^I \theta^I \ , \quad (55)$$

where $a = 1, 2, 3$ and I spans the nodes of the finite element mesh.

In the remainder of this section, the coupling between the momentum and energy equation is delineated in detail. By convention, capital- and lower-case Roman indices are used for referential and spatial components of tensors, while lower-case Greek letters are used for components in the intermediate configuration.

5.1 Linearization of the momentum equations

The linearization of the stress-divergence term in (50) leads to an expression of the form

$$\sum_{I,J} w_a^I \left[(C_{uu})_{ab}^{IJ} \Delta u_b^J + (C_{u\theta})_a^{IJ} \Delta \theta^J \right] \ , \quad (56)$$

where Δu_a^I and $\Delta \theta^I$ denote the increments of the nodal displacements and temperatures, respectively.

Taking into account $(55)_1$, it follows that

$$(C_{uu})_{ab}^{IJ} \;=\; \int_{\Omega_0} N_{,A}^I \frac{\partial P_{aA}}{\partial F_{bB}} N_{,B}^J \; dV \;, \tag{57}$$

where, upon relating the first to the second Piola-Kirchhoff stress,

$$\frac{\partial P_{aA}}{\partial F_{bB}} \;=\; F_{aC} \frac{\partial S_{CA}}{\partial E_{BD}} F_{bD} + \delta_{ab} S_{BA} \;. \tag{58}$$

The first term on the right-hand side of (58) gives rise to the material stiffness, while second term yields the geometric stiffness. Concentrating on the material stiffness, note that the expression for $\mathbf{S}^e$ in (33) for the "FT" model immediately implies that

$$\frac{\partial \mathbf{S}^e}{\partial \mathbf{E}^e} = \mathbb{C} \;. \tag{59}$$

It follows that

$$\frac{\partial S_{\alpha\beta}^e}{\partial E_{CD}} \;=\; \frac{\partial S_{\alpha\beta}^e}{\partial E_{\gamma\delta}^e} \frac{\partial E_{\gamma\delta}^e}{\partial E_{CD}} \;=\; \mathbb{C}_{\alpha\beta\gamma\delta} \big[(F^{t^{-1}})_{C\gamma} (F^{t^{-1}})_{D\delta} \big]^s \;, \tag{60}$$

where the term $[\cdot]^s$ is symmetric with respect to indices {C,D}, and (53) and (54) have been used to eliminate the contribution of the current deformation on $\mathbb{C}$ and $\mathbf{F}^t$. Hence, using (32) one obtains

$$\frac{\partial S_{AB}}{\partial E_{CD}} \;=\; \hat{\mathbb{C}}_{ABCD} \;=\; (F^{t^{-1}})_{A\alpha} (F^{t^{-1}})_{B\beta} \mathbb{C}_{\alpha\beta\gamma\delta} (F^{t^{-1}})_{C\gamma} (F^{t^{-1}})_{D\delta} \;, \tag{61}$$

which is the pull-back of the elasticity tensor $\mathbb{C}$ from the intermediate to the reference configuration.

Likewise, for the "ET" model, the expression (43) leads to

$$\frac{\partial S_{AB}}{\partial E_{CD}} \;=\; \mathbb{C}_{ABCD} \;. \tag{62}$$

Turning now to the coupling between displacements and temperature, recall (33) to conclude that

$$\frac{\partial \mathbf{S}^e}{\partial \theta} \;=\; -\mathbb{C}\mathbf{A} \;, \tag{63}$$

which implies that the tangent term in the momentum equations due to thermal coupling is

$$(C_{u\theta})_a^{IJ} \;=\; -\int_{\Omega_0} N_{,A}^I F_{a\alpha}^e \mathbb{C}_{\alpha\beta\gamma\delta} A_{\gamma\delta} F_{A\beta}^{t^{-1}} N^J \; dV \;, \tag{64}$$

where (32) and (63) are used.

On the other hand, for the "ET" model the expression for stress (43) leads to

$$\frac{\partial \mathbf{S}}{\partial \theta} = -\mathbb{C}\mathbf{A} , \tag{65}$$

therefore

$$(C_{u\theta})_a^{IJ} = -\int_{\Omega_0} N_{,A}^I F_{aB} \mathbb{C}_{BACD} A_{CD} N^J \, dV . \tag{66}$$

5.2 Linearization of the energy equation

The linearizations of the energy equations (51) and (52) lead to terms of the form

$$\sum_{I,J} w^I \left[(C_{\theta u})_a^{IJ} \Delta u_a^J + (C_{\theta\theta})^{IJ} \Delta \theta^J \right] . \tag{67}$$

Two terms in (51) and (52) contribute to $(C_{\theta u})_a^{IJ}$: the first, $(C_{\theta u}^{(t)})_a^{IJ}$ is due to the phase transformation, while the second, $(C_{\theta u}^{(e)})_a^{IJ}$, is due to the thermoelastic coupling. Writing the linearization of the components of the elastic right Cauchy-Green deformation tensor as

$$(DC^e)_{\alpha\beta} = \sum_J 2\left[F_{a\alpha}^e N_{,A}^J (F^{t-1})_{A\beta} \right]^s \Delta u_a^J = \sum_J G_{a\alpha\beta}^J \Delta u_a^J , \tag{68}$$

it follows that for the "FT" model

$$(C_{\theta u}^{(t)})_a^{IJ} = -\int_{\Omega_0} N^I \left[G_{a\alpha\beta}^J S_{\beta\gamma}^e + C_{\alpha\beta}^e \mathbb{C}_{\beta\gamma\delta\epsilon} G_{a\delta\epsilon}^J \right] \tilde{F}_{\alpha\gamma}^t \, dV , \tag{69}$$

where $\tilde{\mathbf{F}}^t = \dot{\mathbf{F}}^t \mathbf{F}^{t-1} = \sum_{\alpha=1}^{nv} \mathbf{H}_\alpha^t \mathbf{F}^{t-1} \dot{\xi}_\alpha$.

For the "ET" model, using (42) and (62), the tangent can be derived as

$$(C_{\theta u}^{(t)})_a^{IJ} = -\int_{\Omega_0} N^I \, \mathbb{C}_{ABCD} F_{aC} N_{,D}^J \dot{E}_{AB}^t \, dV . \tag{70}$$

The second coupling term involves the linearization of $\dot{\mathbf{E}}^e$ in the thermoelastic term

$$\int_{\Omega_0} w \, \dot{\mathbf{E}}^e \cdot \mathbb{C}\mathbf{A}\theta \, dV = \int_{\Omega_0} w \, \dot{E}_{\alpha\beta}^e \mathbb{C}_{\alpha\beta\gamma\delta} A_{\gamma\delta}\theta \, dV , \tag{71}$$

where (54) is used and $\mathbf{A}$ is assumed constant. To obtain the linearization of $\dot{\mathbf{E}}^e$, start by noting that,

$$\dot{E^e}_{\alpha\beta} = \left[F_{a\alpha}^e \dot{F}_{a\beta}^e \right]^s = \left[F_{a\alpha}^e \left(\dot{F}_{aB}(F^{t-1})_{B\beta} + F_{aB}(\dot{F}^{t-1})_{B\beta} \right) \right]^s . \tag{72}$$

Using the identity

$$\dot{\mathbf{F}}^{t-1} = -\mathbf{F}^{t-1}\dot{\mathbf{F}}^t\mathbf{F}^{t-1} , \tag{73}$$

one obtains

$$\dot{E}^e_{\ \alpha\beta} = \left[F^e_{a\alpha} \left(\dot{F}_{aB}(F^{t^{-1}})_{B\beta} - F^e_{a\gamma}(\tilde{F}^t)_{\gamma\beta} \right) \right]^s . \tag{74}$$

Further, upon employing a discrete time integration scheme, the differential part of $\dot{F}_{aA}$ can be expressed in the form $\sum_J c_2 N^J_{,A} \Delta u^J_a$, where c_2 is a factor deduced from the integrator. For the classical implicit Newmark method, it is easy to see that $c_2 = \dfrac{\gamma}{\beta \Delta t}$, where (β, γ) are the two Newmark parameters, such that where $0 < \beta \le 1/2$ and $0 \le \gamma \le 1$. This leads to

$$(D\dot{E}^e)_{\alpha\beta} = \sum_J \left[N^J_{,A}(F^{t^{-1}})_{A\alpha} \dot{F}^e_{a\beta} + F^e_{a\alpha} N^J_{,B}(F^{t^{-1}})_{B\gamma} \left(c_2 \delta_{\gamma\beta} - \tilde{F}^t_{\gamma\beta} \right) \right]^s \Delta u^J_a =$$
$$\sum_J H^J_{a\alpha\beta} \Delta u^J_a . \tag{75}$$

It follows that

$$(C^{(e)}_{\theta u})^{IJ}_a = - \int_{\Omega_0} N^I H^J_{a\alpha\beta} \mathbb{C}_{\alpha\beta\gamma\delta} A_{\gamma\delta} \theta \, dV . \tag{76}$$

For the "ET" model, the tangent involves linearizing $\dot{\mathbf{E}}$ since $\mathbf{E}^t$ can be approximated explicitly similar to (53). This leads to

$$(C^{(e)}_{\theta u})^{IJ}_a = \int_{\Omega_0} N^I \left[N^J_{,A} \dot{F}_{aB} + F_{aA} N^J_{,B} c_2 \right]^s \mathbb{C}_{ABCD} A_{CD} \theta \, dV . \tag{77}$$

With reference to equation (51), the terms that contribute to thermal stiffness in the energy equation for the "FT" model are

$$\int_{\Omega_0} w \, c \, \dot{\theta} \, dV - \int_{\Omega_0} \text{Grad } w \cdot \mathbf{K} \, \text{Grad } \theta \, dV + \int_{\Omega_0} w \dot{\mathbf{E}}^e \cdot \mathbb{C} \mathbf{A} \theta \, dV$$
$$- \int_{\Omega_0} w \left[(\mathbf{C}^e \mathbf{S}^e) \cdot \tilde{\mathbf{F}}^t \right] dV . \tag{78}$$

Noting that the differential of $\dot{\theta}$ in the semi-discrete approximation gives $\sum_J c_2 N^J \Delta \theta^J$, the corresponding tangent terms are obtained in the form

$$(C_{\theta\theta})^{IJ} = \int_{\Omega_0} N^I c N^J c_2 \, dV + \int_{\Omega_0} N^I_{,A} K_{AB} N^J_{,B} \, dV$$
$$+ \int_{\Omega_0} N^I \left(\dot{E}^e_{\alpha\beta} \mathbb{C}_{\alpha\beta\gamma\delta} A_{\gamma\delta} + C^e_{\alpha\beta} \mathbb{C}_{\beta\gamma\delta\epsilon} A_{\delta\epsilon} \cdot \tilde{F}^t_{\alpha\gamma} \right) N^J \, dV , \tag{79}$$

where $(55)_2$ and (63) are used. On the other hand, for the "ET" model, the tangent terms are similarly obtained in the form

$$(C_{\theta\theta})^{IJ} = \int_{\Omega_0} N^I c N^J c_2 \, dV + \int_{\Omega_0} N^I_{,A} K_{AB} N^J_{,B} \, dV + \int_{\Omega_0} N^I \dot{E}_{AB} \mathbb{C}_{ABCD} A_{CD} N^J \, dV , \tag{80}$$

with the aid of $(55)_2$ and (65).

6   Experimental results and numerical simulations

6.1   Simple mechanical simulations to compare models

The difference between the stress response obtained from the "FT" and the "ET" models for mechanical loading under isothermal conditions is highlighted here. The parameters used for these illustrative simulations are the same as for the thin-walled tube case in the ensuing section. A cubic block meshed with one finite element is provided with boundary conditions to prevent rigid body modes and a cyclic tensile loading is applied along one direction so that complete transformation is reached. The stresses attained are similar for the two models upto moderate strains of 5-6%. However, the "ET" model shows hardening in the response from the onset of transformation. This leads to higher differences at large deformations, as seen towards the completion of martensitic transformation in Figure 1.

6.2   Thermomechanical experiments and simulations on thin-walled tube

A set of thermomechanical experiments were used to deduce some of the material parameters and subsequently evaluate the predictive capacity of the two models. The experiments were carried out on thin-walled tubes in tension at strain rates of 10^{-4}/s and 10^{-3}/s under displacement control. The ambient temperature in the experimental facility was set to $\theta_0 = 295$ K. The tubes used in the experiments have an inner diameter of 3.47 mm and constant thickness of 0.45 mm throughout their length of 76.2 mm. The strain rate estimation was based on the initial grip-to-grip length of 76.2 mm. The uniaxial stress was estimated as applied load divided by the undeformed area and the strain was measured by a strain gage in the middle 25.4 mm section of the tube. The temperature was recorded on a thermocouple attached directly to the middle of the tube. Figure 2 illustrates a close-up of the experimental set-up. The experimental protocol of the tensile test was consistent with ASTM F2516. Also, the austenite-finish temperature was estimated from differential scanning calorimetry to be $A_f = 296$ K.

The "FT" and "ET" models of Nitinol single crystal were implemented in FEAP, a general-purpose non-linear finite element code partially documented in [18]. In the simulations, the tube was taken to be entirely fixed at both ends to reproduce the effect of the much stiffer grips. Both conduction and convection heat transfer were accounted for in the simulations. The ends of the tube were assumed to be at the ambient temperature due to the large grips acting as heat sinks, thus resulting in conduction of heat between the tube

and the grips. In addition, the lateral surface of the tube were also exposed to ambient conditions which resulted in convection heat transfer between the tube and the surrounding air. Convection coefficients depend on the placement of the specimen (here, vertical) and are affected by its temperature, owing to the different air flow patterns generated in the vicinity of the tube. A standard assumption is that the normal heat flux can be adequately approximated as $q_n = h(\theta - \theta_0)^n$, see [19]. Here, the value of the exponent is chosen to be $n = 1.25$ based on the geometry and expected temperature of the tube [19, Chapter 7]. The coefficient h also varies with temperature since it affects the properties of the air film surrounding of the tube. By way of simplification, the value of h was assumed constant and equal to 10 for $\theta > \theta_0$ and 80 for $\theta \leq \theta_0$. These values were chose to match the history of tube temperature for the strain rate of 10^{-3}/s. The same parameters were used for the strain rate of 10^{-4}/s and the resulting temperature response appeared to match well the experiments.

The material parameters used for Nitinol are as follows: The austenite and martensite phases were assumed isotropic with respective Young's moduli $E_a = 60.0$ GPa and $E_m = 20.0$ GPa, while the Poisson ratio was $\nu = 0.3$ for both phases. The mechanical parameters were selected to match the loading-unloading curves of tension experiments performed at isothermal conditions for tubes with similar properties in [20]. Also, for the tube used in the experiments, the initial volume fraction of martensite is zero. The thermal conductivity and the thermal expansion were also taken to be isotropic and equal to $K = 18$ W/(m K) and $A = 11 \times 10^{-6}$ /K, respectively, while the volumetric heat capacity was $c = 5.8$ MJ/(m^3 K). These properties are documented in the handbook for NiTi [21] and the technical information available at [22]. Further, the thermodynamic constants for the "FT" model were chosen to be $B = 0.75$ MPa/K, $\theta_T = 268$ K and $\mathcal{F}_c = 3.5$ MPa. On the other hand, for the "ET" model the thermodynamic constants were $B = 0.775$ MPa/K, $\theta_T = 268$ K and $\mathcal{F}_c = 5.0$ MPa. The thermodynamic constants B and $\mathcal{F}_c$ were chosen to match the experimental results, while θ_T was estimated from differential scanning calorimetry data. Although these parameters were calibrated with experimental results at strain rate of 10^{-4}/s where some temperature variations were present, experiments conducted at nearly isothermal strain rates where the forward and reverse transformation plateaus are independent of of temperature variations, will be best suited for this purpose.

The tube mesh was constructed using 420 eight-node brick elements that feature $2 \times 2 \times 2$ integration, see Figure 3. This mesh size was arrived at after considering the issues of accuracy and computational expense. Each element is assumed to represent a crystal,

and all such crystals are oriented according to homogeneous sheet texture, such that the $< 111 >$ austenite lattice vector is aligned with the longitudinal axis of the specimen, as in [9]. This orientation was found to be predominant in the thin-walled tube experiments referred to in this work. Thus, note that the entire effects of polycrystalline texture and that of grain size and shape are not taken into account in this work. The influence of these factors on the thermomechanical response can be accounted for through a multiscale thermomechanical implementation of this algorithm, which is discussed in an upcoming work [23]. The effect of convection was incorporated by superposing 4-node quadrilateral elements with a temperature degree-of-freedom to the outer and inner surfaces of the tube. The tube is loaded to approximately 6% strain and then unloaded back to zero strain.

The uniaxial stress-strain response of the tube under tension is compared in Figure 4 and Figure 5 to the experimental results for strain rates of 10^{-4}/sec and 10^{-3}/sec, respectively. As expected, both experiments and theory predict that the transformation plateau hardens with increasing strain rates due to the higher temperatures attained in the specimen. This can be concluded from (37) since with the increase of temperature, for a given deformation state, forward transformation can only occur at higher stresses. However, for the higher strain rate both models predict stiffer response than the experiments during the phase transformation. This is possibly due to the temperature-dependence of the material properties, which is unaccounted for in the models. Figure 6 and Figure 7 show the temperature history at the middle of the tube for the aforementioned strain rates. Both models are quite close to the experiments and predict the maximum and minimum temperatures with good accuracy. The only deviation of the models from the experiments is the part of the forward transformation, where the formation of R-phase and its subsequent transformation to martensite may be taking place and which is not modeled here. An explicit account of R-phase in the model entails significant added complexity due to the dependence of the rhombohedral angle on temperature, see an earlier effort for the isothermal case [24]. Further, Figure 8 shows the temperature distribution in the tube at end of loading for the two strain rates. As expected, the temperatures are generally lower for the lower strain rate. Also, the effect of conduction on the temperature distribution at the end of loading is more pronounced in the lower strain-rate case (10^{-4}/sec). This is because the rate of heat production due to phase transformation is comparable to the rate at which heat is conducted toward the grips, hence the higher temperatures are confined in the middle of the tube. For the rate of 10^{-3}/sec, in contrast, higher temperatures prevail over a larger section of the tube at the end of loading, since the rate of heat generation is

much higher than the rate at which heat is conducted toward the grips. Here, convection, which occurs through the entire lateral surface of the tube, plays a more prominent role than conduction due to larger temperature deviations from ambient. Figure 9 illustrates the comparison of longitudinal stress distributions at the end of loading for the two strain rates. It is noted that the stresses are quite uniform for both rates, although their values are clearly different. Both temperature and stress results are obtained using the "FT" model, although they are not appreciably different for the "ET" model. However, note that the "ET" model shows a clear trend of more hardening than the "FT" model that would lead to higher differences at large deformations as discussed earlier. Lastly, Figure 10 shows the martensitic volume fractions at the end of loading using the "FT" model. The volume fractions for the strain rate of 10^{-4}/sec are overall higher than those at the strain rate of 10^{-3}/sec, since the lower temperature attained for slower loading is more conducive to transformation, as can be readily concluded from (36) and (37). For the same reason, the volume fractions are higher towards the end of the tube than at the center for both strain rates.

7   Conclusions

Two new models are developed for the fully-coupled thermomechanical response of Nitinol grains. The selection of active variants and the determination of the corresponding volume fractions is effected by a robust algorithmic scheme that couples the transformation equations to the constraints. A monolithic finite element formulation is implemented to address the strong coupling between the thermal and mechanical response. The predictive capacity of the two models is assessed by way of experiments conducted at different strain rates and shown to be good. Further work is needed to characterize the effect of the intermediate R-phase and the possible dependence of material properties on temperature. Also, additional effort is needed to successfully model the effect of texture in the thermomechanical response of Nitinol. Experiments in which the specimen is subjected to different deformation modes and temperature cycles are necessary to adequately validate such models.

References

[1] N. Siredey, E. Patoor, M. Berveiller, and A. Eberhardt. Constitutive equations for polycrystalline thermoelastic shape memory alloys. Part I. Intragranular interactions and behavior of the grain. *Int. J. Solids Struct.*, 36:4289–4315, 1999.

[2] X. Gao and M. Huang and. L.C. Brinson. A multivariant micromechanical model for smas part 1. crystallographic issues for the single crystal model. *Int. J. Plast.*, 16:1345–1369, 2000.

[3] S. Govindjee and C. Miehe. A multi-variant martensitic phase transformation model: Formulation and numerical implementation. *Comp. Meth. Appl. Mech. Engrg.*, 191:215–238, 2001.

[4] E. Patoor, D.C. Lagoudas, P.B. Entchev, L.C. Brinson, and X. Gao. Shape memory alloys, part i: General properties and modeling of single crystals. *Mech. Mater.*, 38:391–429, 2006.

[5] L. Anand and M.E. Gurtin. Thermal effects in the superelasticity of crystalline shape-memory materials. *J. Mech. Phys. Sol.*, 51:1015–1058, 2003.

[6] S. Turtletaub and A.S.J. Suiker. A multiscale thermomechanical model for cubic to tetragonal martensitic phase transformations. *Int. J. Sol. Struct.*, 43:4509–4545, 2006.

[7] E. Stein and G. Sagar. Theory and finite element computation of cyclic martensitic phase transformation at finite strain. *Int. J. Num. Meth. Engrg.*, 74:1–31, 2007.

[8] S. Govindjee and G.J. Hall. A computational model for shape memory alloys. *Int. J. Solids. Struct.*, 37:735–760, 2000.

[9] Y. Jung, P. Papadopoulos, and R.O. Ritchie. Constitutive modelling and numerical simulation of multivariant phase transformation in superelastic shape-memory alloys. *Int. J. Num. Meth. Engrg.*, 60:429–460, 2004.

[10] A. Sengupta and P. Papadopoulos. A note on the use of multiplicative decomposition for displacive phase transformations. *Submitted to Int. J. Engrg. Sci.*, 2010.

[11] J. Mandel. Thermodynamics and plasticity. In *Foundations of Continuum Thermodynamics*, pages 283–304. Macmillan, 1973.

[12] D. Christ and S. Reese. A finite element model for shape memory alloys considering thermomechanical couplings at large strains. *Int. J. Solids. Struct.*, 46:3694–3709, 2009.

[13] P. Thamburaja and L. Anand. Polycrystalline shape-memory materials: Effect of crystallographic texture. *J. Mech. Phys. Sol.*, 49:709–737, 2001.

[14] D. Entemeyer, E. Patoor, E. Eberhardt, and A. Berveiller. Strain rate sensitivity in superelasticity. *Int. J. Plast.*, 16:1269–1288, 2000.

Version: March 15, 2011, 12:27

[15] S. Nemat-Nasser, J.Y. Choi, W.G. Guo, J.B. Isaacs, and M. Taya. High strain-rate, small strain response of a NiTi shape-memory alloy. *J. Engrg. Mater. Tech.*, 127:83–89, 2005.

[16] C. Grabe and O.T. Bruhns. On the viscous and strain rate dependent behavior of polycrystalline NiTi. *Int. J. Solids and Struct.*, 45:1876–1895, 2008.

[17] D. Helm and P. Haupt. Shape memory behaviour: modelling within continuum thermomechanics. *Int. J. Solids and Struct.*, 40:827–849, 2003.

[18] R.L. Taylor. *FEAP - A Finite Element Analysis Program: Users Manual.* University of California, Berkeley, 2008. http://www.ce.berkeley.edu/rlt.

[19] J.P. Holman. *Heat Transfer.* McGraw-Hill, Inc., New York, 1990.

[20] J.M. McNaney, V. Imbeni, Y. Jung, P. Papadopoulos, and R.O. Ritchie. An experimental study of the superelastic effect in a shape-memory nitinol alloy under biaxial loading. *Mech. Mat.*, 35:969–986, 2003.

[21] T.W. Duerig and A.R. Pelton. Ti-Ni shape memory alloys. *Materials Properties Handbook Titanium Alloys*, pages 1035–1048, 1994.

[22] Johnson Matthey Medical. Nitinol technical properties, 2009. http://jmmedical.com/resources/221/Nitinol-Technical-Properties.html.

[23] P. Papadopoulos A. Sengupta and R.L. Taylor. A multiscale finite-element method for modeling fully-coupled thermomechanical problems in solids. to appear in 2011.

[24] A. Sengupta and P. Papadopoulos. Constitutive modeling and finite element approximation of B2-R-B19' phase transformations in Nitinol polycrystals. *Comp. Meth. Appl. Mech. Engrg.*, 198:3214–3227, 2009.

APPENDIX A: Derivation of thermodynamic driving force and its differential for phase transformation model

The free energy for the phase transformation model adopted in this work is given in (31). It follows that

$$
f_\alpha \;=\; -\frac{\partial \hat{\Psi}}{\partial \xi_\alpha} = -\left[\mathbb{C}\left(\mathbf{E}^e - \mathbf{A}(\theta - \theta_0)\right) \cdot \frac{\partial \mathbf{E}^e}{\partial \xi_\alpha} \right] - B(\theta - \theta_T) = -\mathbf{S}^e \cdot \frac{\partial \mathbf{E}^e}{\partial \xi_\alpha} - B(\theta - \theta_T) \,. \quad \text{(A.1)}
$$

Now, using (6) one has

$$
\frac{\partial \mathbf{E}^e}{\partial \xi_\alpha} = \left[\mathbf{F}^{t-T} \mathbf{C} \frac{\partial \mathbf{F}^{t-1}}{\partial \xi_\alpha} \right]^s = \mathbf{G}_\alpha \,. \quad \text{(A.2)}
$$

Using the definition of the transformation deformation gradient in (4), one arrives at

$$
\frac{\partial \mathbf{F}^{t-1}}{\partial \xi_\alpha} = -\mathbf{F}^{t-1} \mathbf{H}^t_\alpha \mathbf{F}^{t-1} \,, \quad \text{(A.3)}
$$

which leads to

$$
\frac{\partial \mathbf{E}^e}{\partial \xi_\alpha} = -\left[\mathbf{F}^{t-T} \mathbf{C} \mathbf{F}^{t-1} \mathbf{H}^t_\alpha \mathbf{F}^{t-1} \right]^s = -\left[\mathbf{C}^e \mathbf{H}^t_\alpha \mathbf{F}^{t-1} \right]^s \,. \quad \text{(A.4)}
$$

Substituting (A.4) in (A.1) leads to an expression for the thermodynamic force as

$$
f_\alpha = \mathbf{S}^e \cdot \left[\mathbf{C}^e \mathbf{H}^t_\alpha \mathbf{F}^{t-1} \right]^s - B(\theta - \theta_T) = (\mathbf{C}^e \mathbf{S}^e) \cdot \left(\mathbf{H}^t_\alpha \mathbf{F}^{t-1} \right) - B(\theta - \theta_T) \,. \quad \text{(A.5)}
$$

To solve the transformation equations (47) incrementally for the potential active variants $\alpha \in \mathcal{PA}$, these equations need to be linearized with respect to the corresponding volume fractions. This, in turn, requires the linearization of the thermodynamic force in (A.5). The differential of this force can be written as

$$
\Delta f_\alpha = - \sum_{\beta \in \mathcal{PA}} \left[(\mathbf{C}^e \mathbb{C} \mathbf{G}_\beta) \cdot \left(\mathbf{H}^t_\alpha \mathbf{F}^{t-1} \right) + 2 (\mathbf{G}_\beta \mathbf{S}^e) \cdot \left(\mathbf{H}^t_\alpha \mathbf{F}^{t-1} \right) + \right.
$$
$$
\left. (\mathbf{C}^e \mathbf{S}^e) \cdot \left(\mathbf{H}^t_\alpha \mathbf{F}^{t-1} \mathbf{H}^t_\beta \mathbf{F}^{t-1} \right) \right] \Delta \xi_\beta \,, \quad \text{(A.6)}
$$

where (A.3) and (A.4) are used. Hence the transformation equations can be written as

$$
\sum_{\beta \in \mathcal{PA}} A_{\alpha\beta} (\Delta \xi_\beta) = b_\alpha \quad , \quad \alpha \in \mathcal{PA} \,, \quad \text{(A.7)}
$$

where

$$
A_{\alpha\beta} \;=\; (\mathbf{C}^e \mathbb{C} \mathbf{G}_\beta) \cdot \left(\mathbf{H}^t_\alpha \mathbf{F}^{t-1} \right) + 2 (\mathbf{G}_\beta \mathbf{S}^e) \cdot \left(\mathbf{H}^t_\alpha \mathbf{F}^{t-1} \right) +
$$
$$
(\mathbf{C}^e \mathbf{S}^e) \cdot \left(\mathbf{H}^t_\alpha \mathbf{F}^{t-1} \mathbf{H}^t_\beta \mathbf{F}^{t-1} \right) \,, \quad \text{(A.8)}
$$

and

$$
\begin{aligned}
b_\alpha &= f_\alpha - \mathcal{F}_c \qquad \text{(forward)} \\
b_\alpha &= f_\alpha + \mathcal{F}_c \qquad \text{(reverse)} .
\end{aligned}
\tag{A.9}
$$

APPENDIX B: Algorithm for Solution of the Transformation Equations

The algorithm used at each integration point to define the set $\mathcal{PA}$ of active variants and compute the corresponding volume fractions is described below:

1. Data: $\mathbf{E}_{n+1}$, θ_{n+1} and the phase transformation state at t_n

2. Calculate $f_{\alpha,n+1}^{(0)}$ and initialize $\mathcal{PA}$ by checking the condition $\mid f_{\alpha,n+1}^{(0)} \mid \geq F_c$.

3. Initialize $i = 1$ and set $\xi_{\alpha,n+1}^{(0)} = \xi_{\alpha,n}, \forall \alpha \in \mathcal{PA}$.

4. Determine $A_{\alpha\beta}^{(i-1)}$ and $b_{\alpha}^{(i-1)}$ and solve (48) for $\Delta\xi_{\alpha,n+1}^{(i-1)}$ and set $\xi_{\alpha,n+1}^{(i)\,TR} = \xi_{\alpha,n+1}^{(i-1)} + \Delta\xi_{\alpha,n+1}^{(i-1)}$.

5. If $\exists\gamma \in \mathcal{PA}$ for which $f_{\gamma,n+1}^{(i-1)}\Delta\xi_{\gamma,n+1}^{(i-1)} < 0$, then

    5a. Remove γ from $\mathcal{PA}$ and go to 4.

6. End if

7. Set $k_1 = k_2 = 1$.

8. If $\sum_{\alpha\in\mathcal{PA}} \xi_{\alpha,n+1}^{(i)\,TR} > 1$, then

    8a. Compute $k_1 = \dfrac{1-\sum_{\alpha\in\mathcal{PA}}\xi_{\alpha,n+1}^{(i-1)}}{\sum_{\alpha\in\mathcal{PA}}\Delta\xi_{\alpha,n+1}^{(i-1)}}$.

9. End if

10. Compute $\xi_{min} = \min_{\alpha\in\mathcal{PA}}\left\{0, \xi_{\alpha,n+1}^{(i)\,TR}\right\}$ and $\alpha_{min} = \mathrm{argmin}_{\alpha\in\mathcal{PA}}\left\{0, \xi_{\alpha,n+1}^{(i)\,TR}\right\}$.

11. If $\xi_{min} < 0$, then

    11a. Compute $k_2 = \dfrac{-\xi_{\alpha,n+1}^{(i-1)}}{\xi_{min}-\xi_{\alpha_{min},n+1}^{(i-1)}}$.

12. End if

13. If $k_1 = k_2 = 1$, then

    13a. Set $\xi_{\alpha,n+1}^{(i)} = \xi_{\alpha,n+1}^{(i)\,TR}$ and exit.

14. Else if $k_1 \leq k_2 \leq 1$, then

    14a. Set $\xi_{\alpha,n+1}^{(i)} = \xi_{\alpha,n+1}^{(i-1)} + k_1\Delta\xi_{\alpha,n+1}^{(i-1)}$ and exit.

15. Else

    15a. Set $\xi_{\alpha,n+1}^{(i)} = \xi_{\alpha,n+1}^{(i-1)} + k_2\Delta\xi_{\alpha,n+1}^{(i-1)}$.

Version: March 15, 2011, 12:27

15b. Drop the variant α_{min} from the set $\mathcal{PA}$, set $i = i + 1$, compute $f_{\alpha,n+1}^{(i-1)}$ and go to step 4.
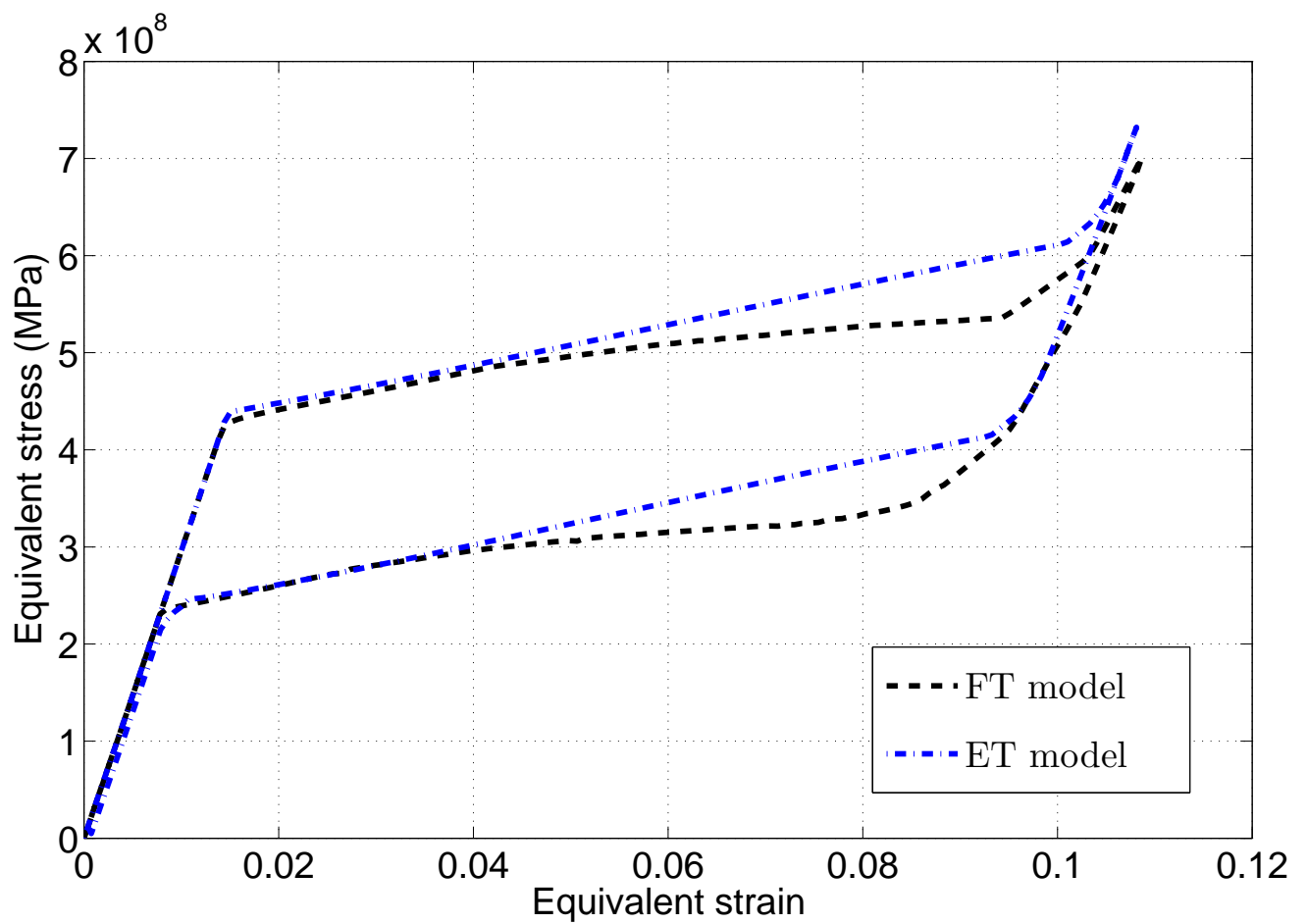
16. End if

Figure 1: *Stress-strain response under cyclic loading of a unit-cube from the two models.*

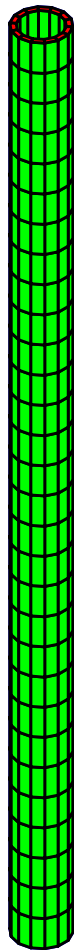Figure 2: *A close-up view of the experimental set-up*

Version: March 15, 2011, 12:27

Figure 3: *Tube mesh comprised of 8-node brick elements*
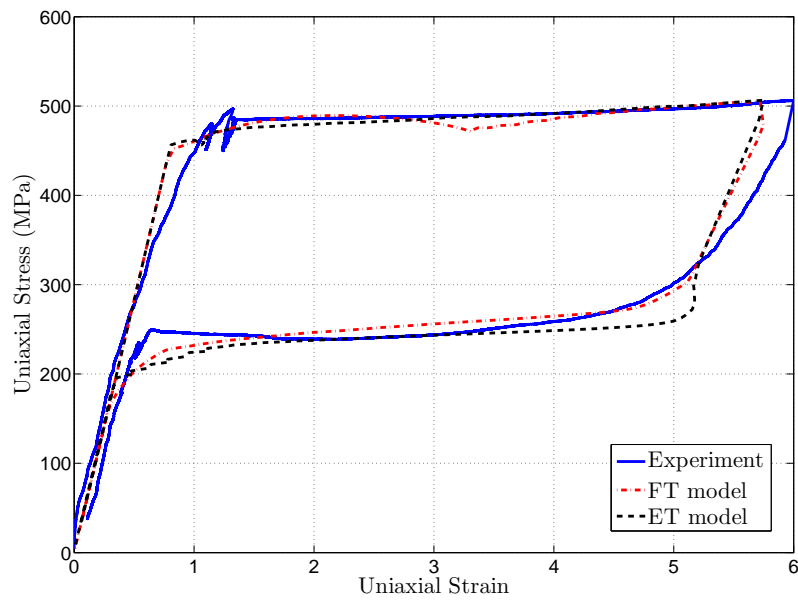
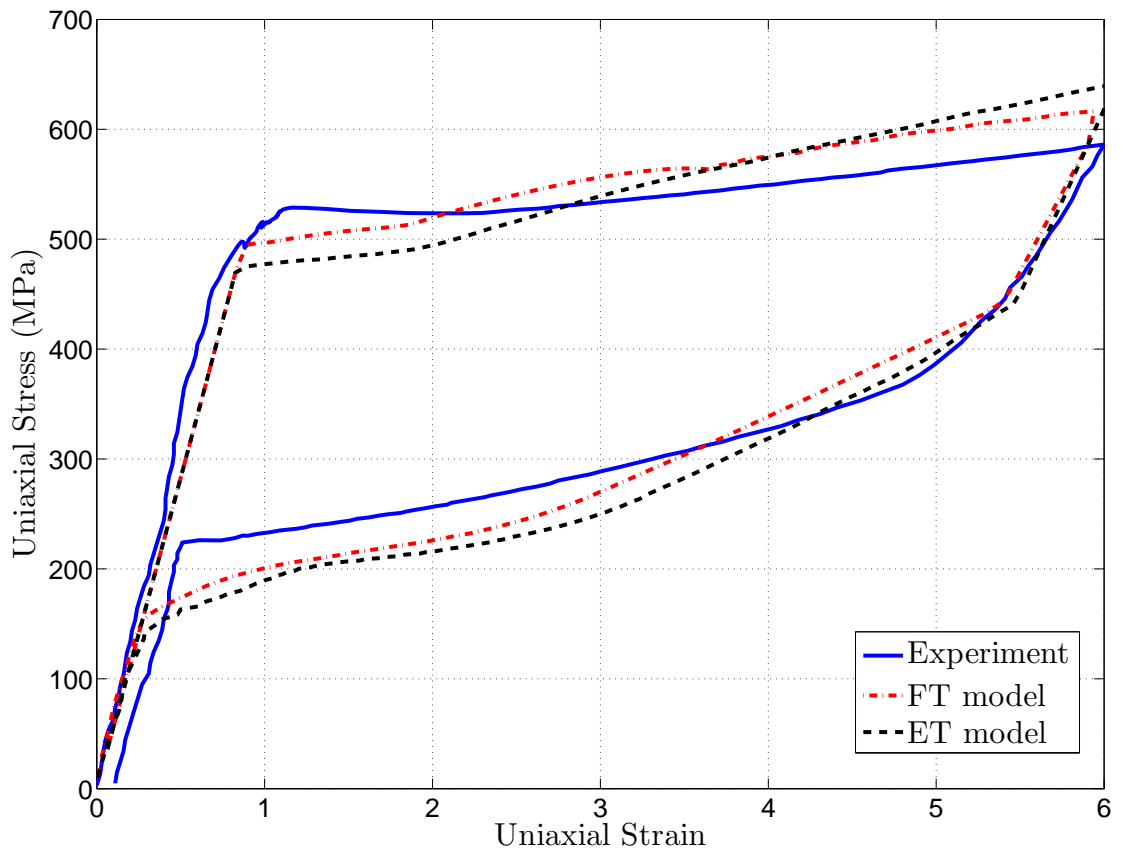Figure 4: *Thin-walled tube in tension: Stress response for strain rate of $10^{-4}/sec$*

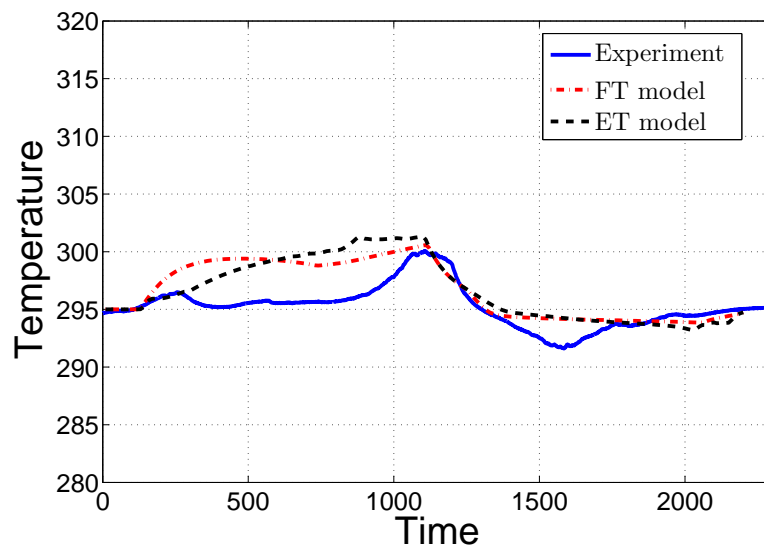Figure 5: *Thin-walled tube in tension: Stress response for strain rate of* $10^{-3}/sec$

Figure 6: *Thin-walled tube in tension: Temperature history at mid-point for strain rate of* $10^{-4}/sec$
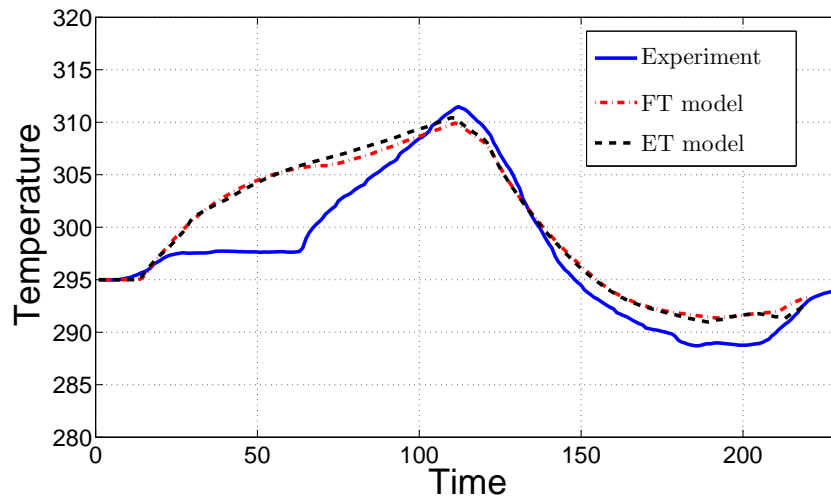
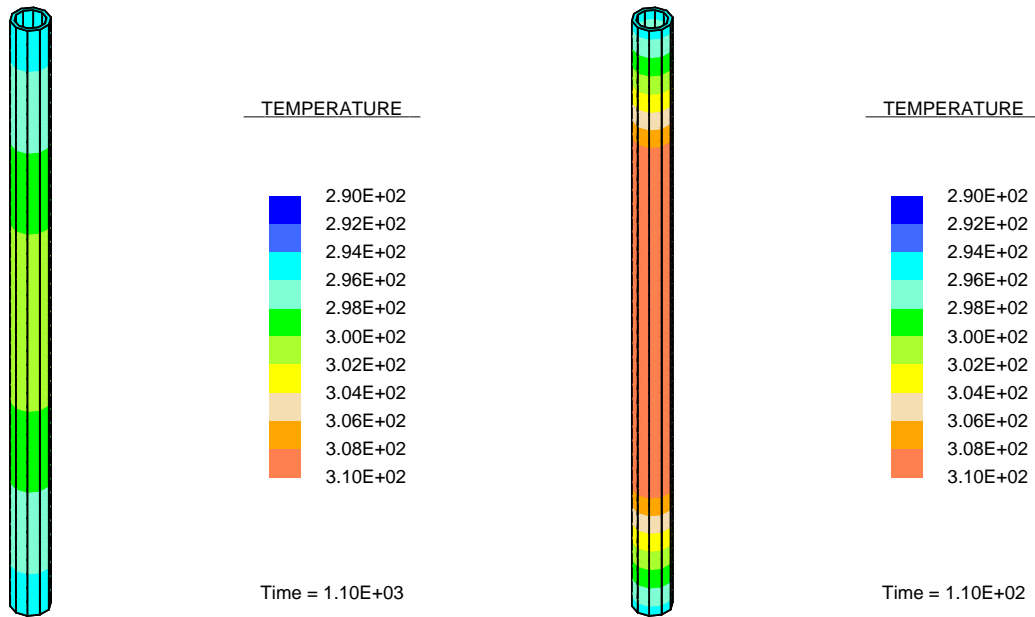Figure 7: *Thin-walled tube in tension: Temperature history at mid-point for strain rate of* $10^{-3}/sec$

Figure 8: *Thin-walled tube in tension: Temperature distributions at the end of loading for strain rates of $10^{-4}/sec$ and $10^{-3}/sec$ using the "FT" model*

STRESS 3

	0.00E+00
	7.55E+07
	1.51E+08
	2.26E+08
	3.02E+08
	3.77E+08
	4.53E+08
	5.28E+08
	6.04E+08
	6.79E+08
	7.55E+08
	8.30E+08
	9.06E+08

Time = 1.10E+03

STRESS 3

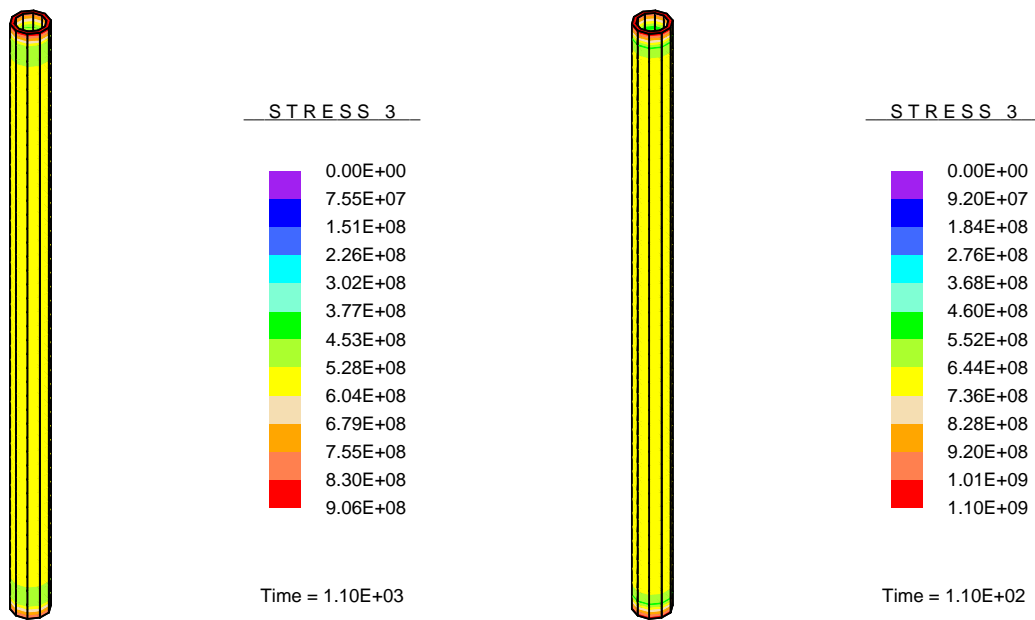|	
	0.00E+00
	9.20E+07
	1.84E+08
	2.76E+08
	3.68E+08
	4.60E+08
	5.52E+08
	6.44E+08
	7.36E+08
	8.28E+08
	9.20E+08
	1.01E+09
	1.10E+09

Time = 1.10E+02

Figure 9: *Thin-walled tube in tension: Longitudinal stress distributions at the end of loading for strain rates of $10^{-4}/sec$ and $10^{-3}/sec$ using the "FT" model*
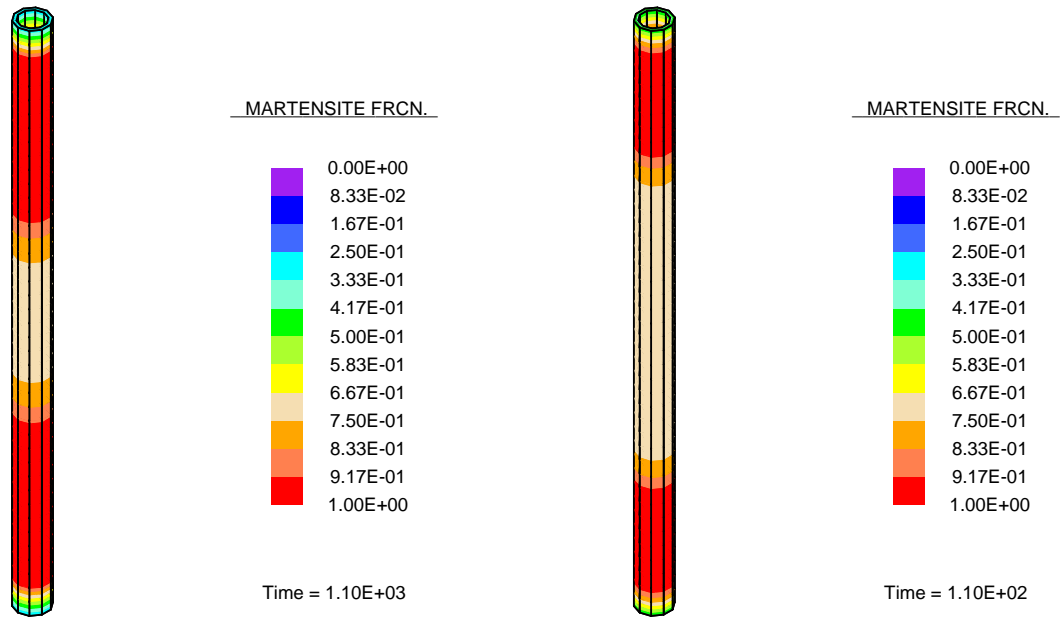
Figure 10: *Thin-walled tube in tension: Martensite volume fractions at the end of loading for strain rates of $10^{-4}/sec$ and $10^{-3}/sec$ using the "FT" model*